Atomically dispersed Fe-N-P-C complex electrocatalysts for superior oxygen reduction

Yahao Li[a,#], Bingxu Chen[a,b,#], Xuezhi Duan[b], Shuangming Chen[c], Daobin Liu[c], Ketao Zang[d], Rui Si[e], Fengliu Lou[a], Xuehang Wang[a], Magnus Rønning[a], Li Song[c,*], Jun Luo[d,*], De Chen[a,*]

[a] Department of Chemical Engineering, Norwegian University of Science and Technology, N-7491 Trondheim, Norway.

[b] State Key Laboratory of Chemical Engineering, East China University of Science and Technology, 130 Meilong Road, Shanghai 200237, China.

[c] National Synchrotron Radiation Laboratory, CAS Center for Excellence in Nanoscience, University of Science and Technology of China, Hefei, Anhui 230029, China.

[d] Center for Electron Microscopy and Tianjin Key Lab of Advanced Functional Porous Materials, Institute for New Energy Materials, School of Materials, Tianjin University of Technology, Tianjin 300384, China.

[e] Shanghai Synchrotron Radiation Facility, Shanghai Institute of Applied Physics, Chinese Academy of Sciences, Shanghai 201204, China

[#] These authors contributed equally to this work.

[*]Corresponding Authors. E-mail: chen@nt.ntnu.no; song2012@ustc.edu.cn; jluo@tjut.edu.cn.

Abstract

Development of cost-effective electrocatalysts as the alternative to platinum for oxygen reduction reaction (ORR) is of great significance for boosting the applications of green energy devices such as fuel cells and metal-air batteries. Here we report a general approach to synthesize a new type of iron, nitrogen and phosphorus tri-doped hierarchically porous carbon composite derived from biomass. This low-cost composite outperforms most of state-of-the-art ORR catalysts in alkaline electrolyte. Aberration-corrected HAADF-STEM, XPS and XAFS measurements reveal the atomically dispersed Fe-N-P-C complex as dominant active sites for ORR. Combining structure characterization by XAFS results with DFT calculations, a new molecule-like structure is proposed where the associated Fe-O-P bond can significantly lower the stability of strongly adsorbed O* and OH* on the catalytically active sites and thus give rise to enhanced ORR performance. Fe is identified as the main active canter and its ORR activity is clearly correlated to the charge of Fe, which is controlled by the local surrounding structure in the active site. It rationalizes the outperformance of Fe-N-P-C than Fe-N-C, and N-C. The insights reported here open a new avenue for constructing highly efficient molecule-like heterogeneous catalysts in electrochemical energy technologies.

Introduction

Electrochemical reduction of oxygen, also known as oxygen reduction reaction (ORR), normally determines the efficiency of energy conversion and storage systems such as fuel cells and metal-air batteries, where the cost-effective catalysts are essential for their practical applications [1-5]. Complete oxygen reduction involves the transfer of four electrons with the cleavage of the O-O bond and the maximum release of energy [6,7]. Great efforts have been devoted to reduce the

overpotential of ORR catalysts. One strategy is to increase the utilization efficiency of commonly used, highly active platinum-based ORR catalysts by increasing the proportion of Pt atoms exposed on the surface (i.e., the number of active sites) and/or enhancing the intrinsic activity of the active sites [8-11]. Another strategy is to develop alternative electrocatalysts such as metal-free [12-15] or precious-metal-free [16-20] materials with comparable or even better ORR performance. Among them, nanocarbons have been demonstrated to be one of the most promising class of ORR catalysts, and their electrocatalytic performance can be further enhanced by introducing heteroatoms to modify the electronic and geometric structures [5,15,20-22]. In particular, Fe-N-C complex catalysts have been reported as possible replacement of Pt-based catalysts [20,22-24]. Thus, rational design of carbon-based ORR catalysts with low cost as well as high activity, selectivity and durability is of great significance.

For ORR in alkaline media, recent work [25,26] highlighted the significance of electronic structure of metal in oxide in controlling the competition between O_2^{2-} /OH^- displacement and OH^- regeneration on metal ions as the rate-limiting steps of the ORR. Inspired by natural catalysts, such as cytochrome c oxidase [27], molecular catalysts, such as macrocyclic MN4 metal complexes confined to electrode surfaces were also investigated and a ORR volcano plot between the ORR activity and M^{III}/M^{II} redox potential of MN4 chelates or the M-O_2 binding energies [28] was established. Similar to heterogeneous catalysis, a proper adsorption strength of the reactant is required, which is typically governed by the electronic properties of metal ions in the active centre. However, efficiently tuning the electronic properties of the active sites to enhance the performance of ORR catalysts remains a challenge.

Herein, we report a simple and easy to scale-up impregnation-pyrolysis route to produce Fe, N and P tri-doped biomass derived porous carbon electrocatalyst (Fe-NPC) with unique atomically

dispersed Fe-N-P-C complex active sites. The as-prepared cost-effective catalyst exhibited remarkable ORR activity, long-term cycling stability and methanol tolerance in alkaline electrolyte, and outperformed commercialized Pt/C catalysts. With the help of advanced characterization such as aberration corrected HAADF-STEM and XAFS as well as systematic DFT calculations, the molecule-like structure of the complex was revealed as an active centre, in which the associated Fe-O-P bond significantly lower the stability of strongly adsorbed O* and OH* on the catalytically active sites and thus facilitated the oxygen reduction.

Experimental

Iron, nitrogen and phosphorus tri-doped wood briquette (WB) derived porous carbon electrocatalyst (Fe-NPC) was produced by an impregnation-pyrolysis method. The Norwegian WB was purchased from local supermarket. The properties of WB are presented in the supporting information. Firstly, 6g of WB was dispersed in 200 mL precursor solution, which contained 1.5 mol/L of H_3PO_4 and 0.025 mol/L of $FeCl_3$, and vigorously stirred for 30 minutes. The resulted suspension was filtered with a vacuum filtration set-up and the filter cake was transferred onto a plastic sheet to dry overnight at room temperature. The dried sample was then transferred into a fix-bed reactor, heated to 1000 °C with a heating rate of 5 °C/min and kept for 2 hours under an NH_3 flow with a flow rate of 50 mL/min. After cooling to room temperature in an Ar flow, the obtained black powder was reflux in distilled water overnight to remove any residues. After wash and dry, the Fe-NPC powder was obtained. To compare with, carbonized WB (CWB) were produced by simply carbonized WB powders under an Ar flow at 1000 °C for 2 h.

To compare the effects of different possible active sites, Fe-NPC-L was produced with the same method, and the concentration of $FeCl_3$ in the precursor solution was controlled to be 0.25 mmol/L.

N and P co-doped WB derived carbon electrocatalyst (NPC) was produced also using the impregnation-calcination method, where 1.5 mol/L of H_3PO_4 solution was used as the precursor solution. Fe_xP/C composite was prepared with sodium alginate (SA), $FeCl_3$ and H_3PO_4 as the precursors for C, Fe and P, respectively. SA was firstly dissolved in distilled water to form a 15 wt% gel-like solution. 50 g of this solution was added dropwise into 200 mL solution containing 0.1 mol/L of $FeCl_3$ and H_3PO_4. As the SA coordinated with Fe^{3+}, each drop solidified into a hollow particle. These particles were kept steady in the solution overnight and then dried at 80 °C for 12 h. As-obtained particles were transferred into a fix-bed reactor and heat treated under inert atmosphere at 800 °C for 1 h. After cooling to room temperature, the reactor was reheated to 1000 °C under NH_3 flow and kept for another 1 h. The powder obtained was also refluxed in distilled water overnight. Resulted materials is denoted as Fe_xP/C. Fe and N co-doped WB derived carbon (Fe-NC) was also produced with the impregnation-pyrolysis method, in which 0.25 mmol/L $FeCl_3$ alone was used as precursor solution.

Field emission scanning electron microscopy (FE-SEM, Q-200, Hillsboro, USA) was used to investigate the surface morphologies. Transmission electron microscopy (TEM) characterizations were conducted using a JEM-2100F (JEOL Ltd, Japan) with an accelerating voltage of 200 kV. The high angle annular dark field (HAADF) scanning transmission electron microscopy (STEM) images and element mappings were taken using aberration corrected FEI Titan Cubed Themis G2 300 with an accelerating voltage of 200 kV. The N_2 sorption isotherms were performed on a Tristar II 3020 (Micromeritics Instruments, USA). Pore size distribution (PDS) was obtained from the isotherm results based on DFT calculation. A degassing step was applied to the catalysts at 200 °C for 12 h under turbomolecular vacuum pumping before the adsorption/desorption measurements. Temperature programmed oxidation (TPO) was carried out with a TG/DSC (STA449C,

NETZSCH, USA). X-ray diffraction (XRD) of Fe-NPC was performed using a Bruker D8 Advance DaVinci X-ray diffractometer with Cu Kα radiation (λ = 1.54 Å). X-ray fluorescence (XRF) was carried out using a Supermini 200 (Rigaku, Japan). X-ray photoelectron spectrometry (XPS) was performed using a Kratos XSAM 800 spectrometer (Manchester, UK) equipped with an Al Kα X-ray (1486.6 eV, excitation source working at 15 kV). The C 1s peak at 284.6 eV was taken as an internal standard to correct the shift in the binding energy caused by sample charging. Fe *K*-edge X-ray absorption fine structure (XAFS) spectra were acquired at beamline 14W1 in Shanghai Synchrotron Radiation Facility (SSRF), China, using Si (111) double-crystal monochromator in transmission mode. The storage ring of SSRF was operated at 3.5 GeV with the current of 300 mA. The energy position was calibrated with a Fe foil. The raw data were processed according to the standard procedures using the WinXAS3.1 program [29]. Theoretical amplitudes and phase-shift functions were calculated with the FEFF8.2 code [30]. X-ray absorption near edge structure (XANES) spectroscopy of N *K*-edge and P $L_{2,3}$-edge were performed at the MCD endstation at the beamline BL12B-a in the National Synchrotron Radiation Laboratory (NSRL), Hefei, China. The storage ring of the NSRL was operated at 0.8 GeV with a maximum current of 300 mA. The spectra were recorded at room temperature with an energy step of 0.2 eV and the total electron yield (TEY) detection mode.

The electrochemical oxygen reduction properties of as-obtained catalysts were evaluated with a three-electrode system at ambient condition using a Princeton VersaSTAT potentiostat analyzer (Princeton Applied Research). The working electrode was prepared by coating a catalyst film onto a glassy carbon rotating-disk electrode (RDE, with a diameter of 5 mm). The catalyst ink used in the coating was produced by dispersing 4 mg of catalyst in 2 mL of ethanol solution containing 16 μL of 5 wt% Nafion (Alfa Aesar, D520 dispersion) and sonicated for 120 min. 50 μL of the as-

obtained catalyst ink was coated onto the glassy carbon disk drop by drop, and the as-obtained electrode (about 0.5 mg/cm^2) was dried at room temperature overnight. The counter and reference electrodes are Pt wire and Ag/AgCl electrode (3.5 mol/L KCl) respectively. 0.1 mol/L KOH aqueous solution was used as electrolyte. Argon or oxygen was bubbling into the electrolyte 30 min prior the electrochemical tests according to the demands. To compare with, a Pt/C (30 wt% Pt on Vulcan carbon black, Fuel Cell Store) coated glassy carbon electrode was also prepared according to the same procedure described above, 10 μL of the catalyst ink was used during the coating procedure. All measured potentials were converted to potential vs. reversible hydrogen electrode (RHE) according to the following equation, unless specified [15,19]:

$$E_{vs\ RHE} = E_{vs\ Ag/AgCl} + E_{ø\ Ag/AgCl} + 0.059\ pH$$

Where $E_{\text{vs RHE}}$ is the potential vs. RHE, $E_{\text{vs Ag/AgCl}}$ is the potential vs. Ag/AgCl and $E_{ø\ \text{Ag/AgCl}}$ is the potential of Ag/AgCl electrode respect to the standard hydrogen electrode. The Koutechy-Levich (K-L) equation was used to calculate the electron transfer number (n) per oxygen molecule in ORR process at the electrode [15,31]:

$$\frac{1}{J} = \frac{1}{J_L} + \frac{1}{J_K} = \frac{1}{B\omega^{½}} + \frac{1}{J_K}$$

$$B = 0.2nFC_0(D_0)^{2/3}\nu^{-1/6}$$

Where J is the measured current density, J_L is the diffusion limiting current density, J_K is the kinetic limiting current density, ω is the rotating speed in rpm, F is the Faraday constant (96485 C mol^{-1}), D_0 is the diffusion coefficient of oxygen in 0.1 mol/L KOH (1.9×10^{-5} cm^2 s^{-1}), ν is the kinetic viscosity (0.01 cm^2 s^{-1}), and C_0 is the buck concentration of oxygen (1.2×10^{-3} mol L^{-1}).

Results and discussion

The electrocatalytic properties of Fe-NPC were investigated, and the results are presented in Figure 1 and Figure S1 in supplementary information. Figure S1 demonstrated the CV curves of Fe-NPC and CWB in Ar-saturated or O_2-saturated 0.1 mol/L KOH aqueous solution at a scan rate of 10 mV/s. Distinct reduction peaks can be observed only in the O_2-saturated electrolyte, suggesting the abilities of these materials to catalyse oxygen reduction. Moreover, the ORR peak position of Fe-NPC, which is about 270 mV more positive than that of CWB, is similar to that of 30 % Pt/C, indicating outstanding electrocatalytic activity of Fe-NPC towards oxygen reduction. Linear sweep voltammetry (LSV) tests were carried out and the obtained curves are shown in Figure 1a. The pure carbon CWB exhibited a poor ORR activity, almost inert for ORR, while the ORR activity of carbon doped with Fe, N and P (Fe-NPC) was enhanced remarkably, which is superior to the activity of 30 % Pt/C. For a better comparison, the onset potentials (E_{onset}) and half-wave potentials (E_{half}) of each catalyst obtained from the LSV curves are presented in Figure 1b. Both E_{onset} and E_{half} of Fe-NPC are clearly more positive than those of 30 % Pt/C. We also compared our results with recently reported electrocatalysts, as shown in Table S1. It is clearly demonstrated that our electrocatalysts possess among the best ORR activities.

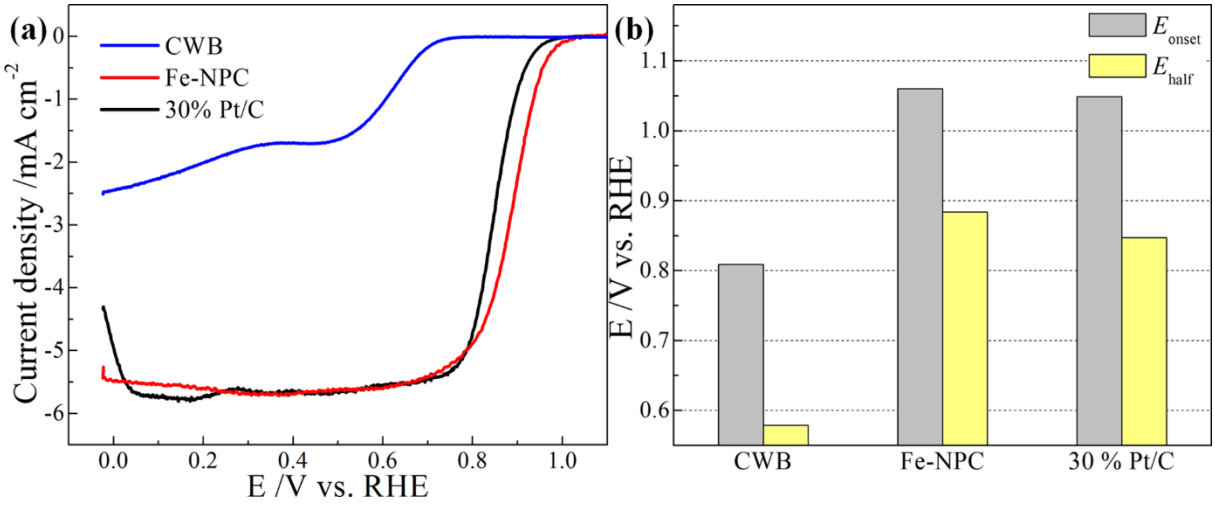

Figure 1. (a) LSV curves of Fe-NPC, CWB and 30 % Pt/C in O_2-saturated 0.1 mol/L KOH at a scan rate of 10 mV/s with a rotating rate of 1600 r.p.m. (b) Bar chart of E_{onset} and E_{half} of Fe-NPC, CWB and 30 % Pt/C.

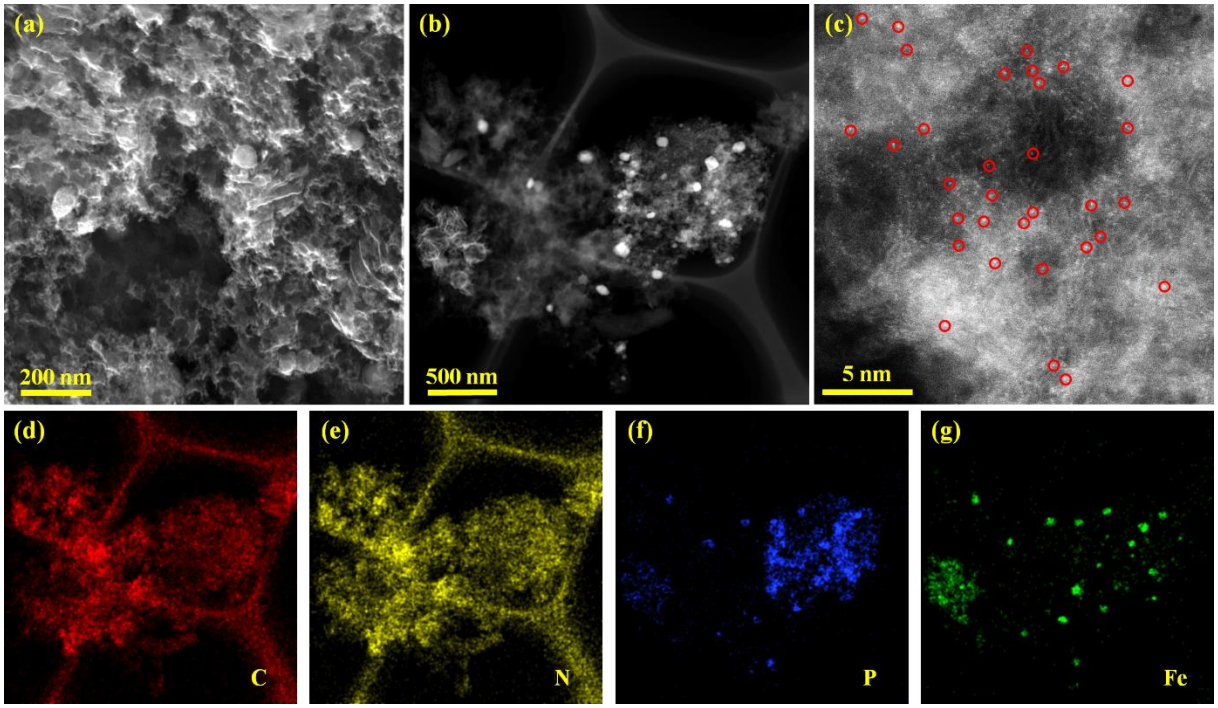

Figure 2. (a) SEM image of Fe-NPC. (b and c) Aberration-corrected HAADF-STEM images of Fe-NPC, in which some of the isolated Fe atoms are highlighted by red circles in (c). Element mapping of (d) C, (e) N, (f) P and (g) Fe correlated to (b).

To reveal the origin of the outstanding ORR activity of Fe-NPC, different characterizations were carried out. The typical SEM image of Fe-NPC (Figure 2a) shows highly porous structure with rough surface. Aberration-corrected HAADF-STEM images of Fe-NPC are shown in Figures 2b and 2c, where the element mappings of C, N, P and Fe of the sample in Figure 2b are shown in Figures 2d, 2e, 2f and 2g, respectively. The N dispersion is basically overlapped with the C dispersion, indicating the evenly doping of N on the carbon body. Meanwhile, P either disperses

on the carbon body or concentrates at where the particles located. In addition, Fe is also concentrated at particle areas in the mapping. These results suggest the successfully doping of N and P onto the carbon body and the particles existing in the catalyst should be compounds composed of Fe and P. The Fe containing particles is about 100 nm, as it is also shown in the TEM images (Figure S2). A higher magnification TEM image (Figure S2b) demonstrates that these particles are encapsulated by carbon layers. Furthermore, the high-magnification observations (Figure 2c) reveals that a significant number of Fe single atoms (partially indicated by red cycles) exist on Fe-NPC. The results indicate that Fe in Fe-NPC also has two types of existence form: particles and single atoms.

N_2 sorption analysis of Fe-NPC was carried out, and the resulted isotherms are shown in Figure S3a. The isotherm curve of Fe-NPC has a similar shape with type I isotherm, indicating that Fe-NPC is micropore abundant material. The pore size distributions (PSDs) of Fe-NPC is shown in Figure S3b. The peak of the PSD curve of Fe-NPC is at around 2 nm with 2 shoulders at around 1.6 and 2.7 nm, respectively. Fe-NPC possesses a SSA of 1361 m^2/g, a mesopore volume of 0.24 cm^3/g and a micropore volume of 0.37 cm^3/g. The resultys suggest the formation of hierarchically porous structures, which is believed to be beneficial to the mass transfer and access of the active sites during oxygen reduction [19]. The XRD curves of Fe-NPC is shown in Figure S3c, where clear peaks ascribed to FeP or Fe_2P are found. Combining XRD and TEM observations, particles presented can be ascribed to iron phosphides, which are reported to possess reasonable ORR activities when encapsulated by carbon layers [32-35]. Moreover, the Fe and P loading of Fe-NPC were obtained from TPO and XRF analysis, which are calculated to be 2.67 wt % and 1.83 wt %, respectively.

The results of XPS analysis of Fe-NPC are shown in Figure 3. Sharp peaks of C 1s and O 1s can easily be observed from the survey curve (Figure 3a), while the peaks for N 1s and P 2p is much smaller. The elemental concentrations of Fe-NPC are shown in Table S2, where C, N, P and Fe atomic percentages are 88.35, 2.16, 7.44, 0.42 and 0.58, respectively. The deconvolutions of N 1s,

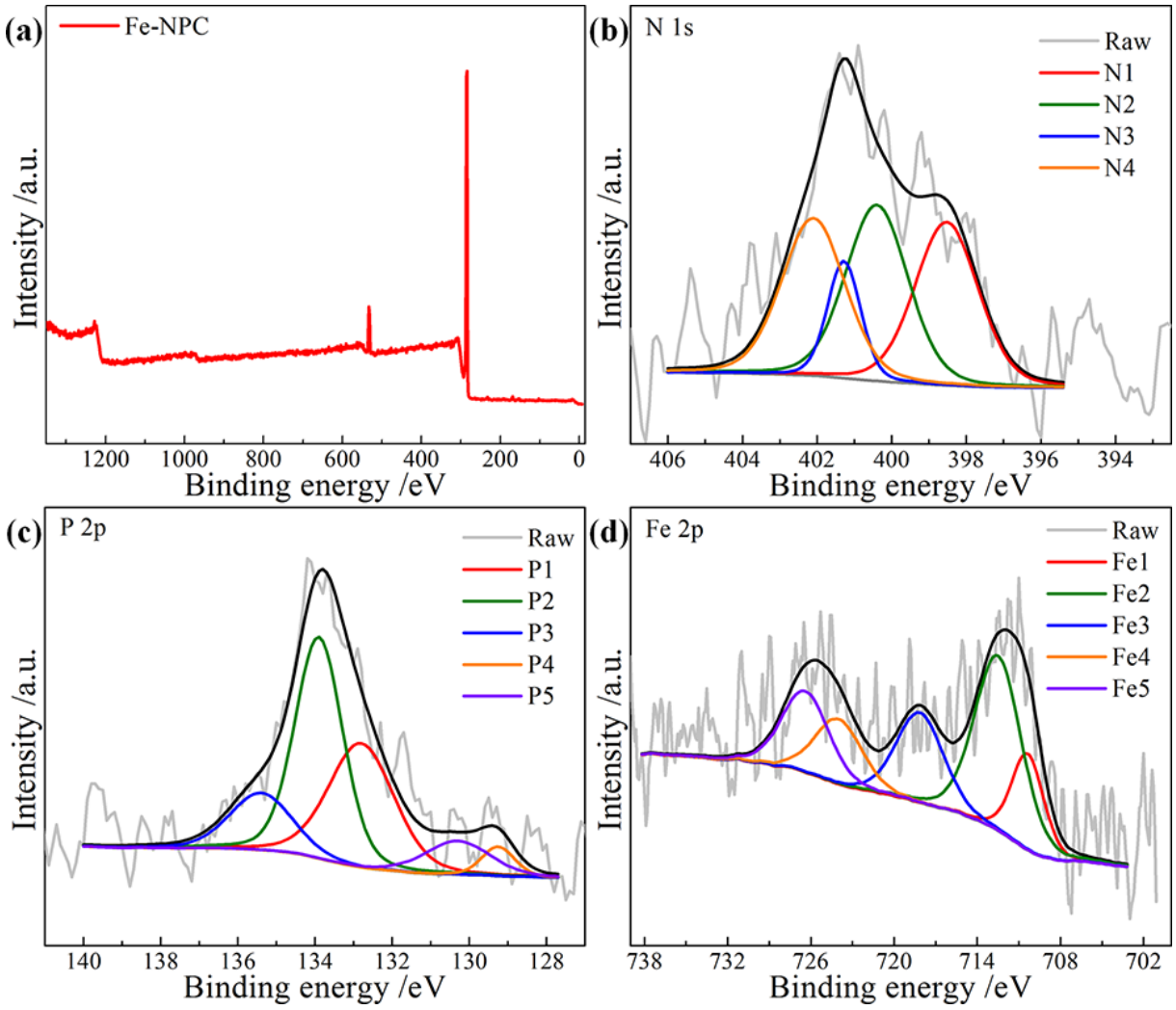

Figure 3. (a) XPS survey, (b) N 1s peak, (c) P 2p peak and (d) Fe 2p peak of Fe-NPC.

P 2p and Fe 2p peaks of Fe-NPC were carried out, as shown in Figures 3b-d. The concentrations of each component peaks (in at%) are summarized in Table S3. N 1s peak can be fitted into four peaks located at around 398.6, 400.5, 401.3 and 402.0 eV, which correspond to pyridinic N (N1),

pyrrolic N (N2), graphitic N (N3) and oxidized pyridinic N (N4), respectively [15]. For Fe-NPC, the concentration for N1 and N2 are similar, and the existence of pyridinic N (N1) is reported to be highly related to the activity of the catalysts towards oxygen reduction [14,15,36]. P 2p peaks can be deconvoluted into five peaks locate at around 132.9, 133.8, 135.5, 129.3 and 130.2 eV, which are aroused by P-C bond (P1), P-O bond (P2), metaphosphate (PO_3^-, P3), P $2p_{3/2}$ of P-Fe (P4) and P $2p_{1/2}$ of P-Fe (P5), respectively [17,37,38]. The present of P1 peak suggests that P is successfully doped into carbon body of Fe-NPC, while the existences of P4 and P5 suggest the present of P-Fe bond, which are possibly ascribed to the Fe_xP particles. In the Fe 2p region, clear peaks for Fe $2p_{3/2}$ and Fe $2p_{1/2}$ can be found in Fe-NPC spectrum. These two peaks can be fitted into five peaks located at around 710.5 eV, 712.5 eV, 718 eV, 724.2 eV and 726.2 eV, which are ascribed to the Fe $2p_{3/2}$ of Fe^{2+} (Fe1) and Fe^{3+} (Fe2), satellite peak of $Fe2p_{3/2}$ (Fe3) and Fe $2p_{1/2}$ of Fe^{2+} (Fe4) and Fe^{3+} (Fe5), respectively [39,40]. No peaks for element Fe can be found. These results suggest that the Fe single atoms displayed in Figure 2c are existed in the form of bivalent and/or trivalent ions.

The synchrotron-based X-ray absorption fine structure spectroscopy (XAFS) technique was employed to acquire more information on the local structure and bonding of the absorbing atom in as-prepared catalysts. Figure 4a shows the normalized Fe K-edge XANES spectra of Fe-NPC, and reference materials of Fe2O3, Fe3O4, FeP, iron phthalocyanine (FePc) and Fe foil. For a clarity purpose, the spectra of the reference materials, a comparison of Fe-NPC with FePc and a comparison of Fe-NPC-L with FeP and FePc are presented in Figure S10, S11 and S12, respectively. In their corresponding first derivative analysis in Figure 4b and Figure S10, the existence of small pre-edge featured at 7112.5 eV in FePc is attributed to a dipole-forbidden but quadrupole-allowed 1s→3d transition in a square planar of FeN_4 [41]. The pre-edge of Fe-NPC located the similar position, but the intensity is much higher compared to the one of FePc (Figure

4b and Figure S11b). In the absorption edges (~7120-7140 eV), FePc reference exhibits the most dominant feature of several 1s → 4p transitions, which are characteristic of an iron (II) complex with square-planar configuration [42,43]. The adsorption edge of Fe-NPC exhibited completely

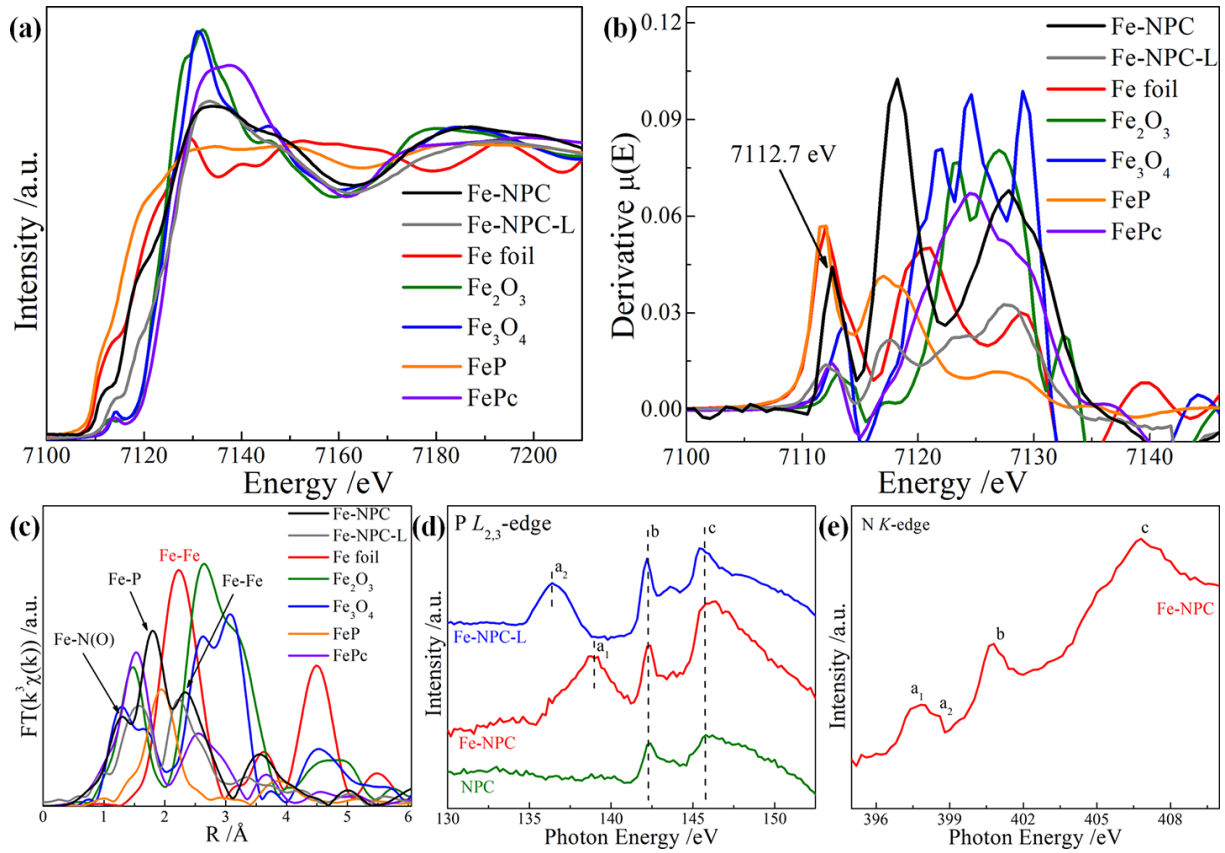

Figure 4. (a) Fe *K*-edge XANES spectra, (b) corresponding first derivative analysis and (c) the k^3 weighted χ(k) function of the EXAFS spectra for Fe-NPC, Fe-NPC-L, Fe foil, Fe_2O_3, Fe_3O_4, FeP and FePc. (d) P $L_{2,3}$-edge XANES spectra of Fe-NPC, Fe-NPC-L and NPC. (e) N *K*-edge XANES spectra of Fe-NPC.

different from the FePc (Figure S11). Both pre edge and adsorption edge located between Fe and Fe (II) in the FeN_4. It clearly reveals a new structure of active site instead of FeN_4 on Fe-NPC.

For the analysis of extended X-ray absorption fine structural (EXAFS) spectroscopy, Fourier transformations (FT) of the k^3-weighted EXAFS functions observed for Fe-NPC and reference compounds are shown in Figure 4c. A comparison of EXAFS spectra between Fe-NPC and Fe-Pc is presented in Figure S11c, which further confirms a different surrounding structure of Fe in Fe-NPC compared to the one in Fe-Pc. The first peak at around 1.30 Å in Figure 4c and Figure S11 for Fe-NPC could be assigned to the Fe-N/O distance, suggesting the existence of the Fe-N_x coordination. The second peak appeared at around 1.80 Å, which is shorter than the Fe-P distance in FeP (~ 1.94 Å, Figure 4b green curve) and longer than the Fe-P distance in Fe_2P (1.75 Å) [44]. This peak can be ascribed to Fe-P coordination in Fe-NPC. The third peak (~2.34 Å) is ascribed to Fe-Fe distance, which is slightly shifted from the Fe-Fe distance of element Fe (~2.23 Å) to that of Fe_2O_3 (~2.64 Å). This could be the evidence of the existence of iron oxide with low valent Fe, which may be the result of mild oxidation when the catalyst contacted with air. Combining the XPS and EXAFS characterizations, Fe single atoms may coordinate to N and P simultaneously, and N and P are both binding to C.

Figure 4d shows a completely distinct P $L_{2,3}$-edge XANES spectra for each catalyst after the phosphorus modification. A broad and intense peak (peak c) at 145.8 eV can be observed in all spectra, owing to the 2p to 3d transitions in phosphorous [45]. The feature (peak b) at 142.3 eV may be ascribed to the P-C/N bonds, suggesting the P heteroatom was successfully doped into carbon matrix [46]. More interestingly, the Fe-NPC catalyst shows another peak (peak a_1) at 138.8 eV with a weak shoulder compared to that of NPC, which is attributed to the transitions to 3p orbitals. It is possible due to the mixed characters from oxygen or metals and forms the Fe-O-P bond [47,48]. Notably, we have used the total electron yield (TEY) mode to collect all XANES spectra, which is sensitive to the surface with detection depth ~5-10 nm [49]. Thus, the iron phosphate could be

detected in the Fe_xP-contained Fe-NPC catalyst due to the surface oxidation in the air. When the Fe content in the catalyst was reduced to form the atomically dispersed catalyst (Fe-NPC-L), the peak was shifted to the lower energy side at 136.4 eV (peak a_2). It is mainly due to the increase in more covalent P-C bonds when the Fe atoms were trapped into carbon matrix in the isolated form. The C atoms possesses smaller electronegativity than the O atom, where the change in the degree of covalence of the P-O bond altered by more contributions of P-C bonds. This result is further confirmed by XPS in Figures 3c and S4c.

N *K*-edge XANES spectra in Figure 4e reflects the unoccupied N 2p electronic states. The peaks at about 398.2 eV (peak a) is assigned to π* transition to pyridinic state, while other two peaks at 401.0 eV (peak b) and 406.9 eV (peak c) are assigned to graphitic N and C-N σ* transitions, respectively [50]. Noteworthy, the peak a splits into double peaks (labelled as $a_1$and a_2) suggests that Fe is bonded to pyridinic N, agreeing with the previous report [51]. These results are also consistent with XPS data that confirmed the Fe existence. Thus, a unique active site consists of Fe-N, Fe-P,

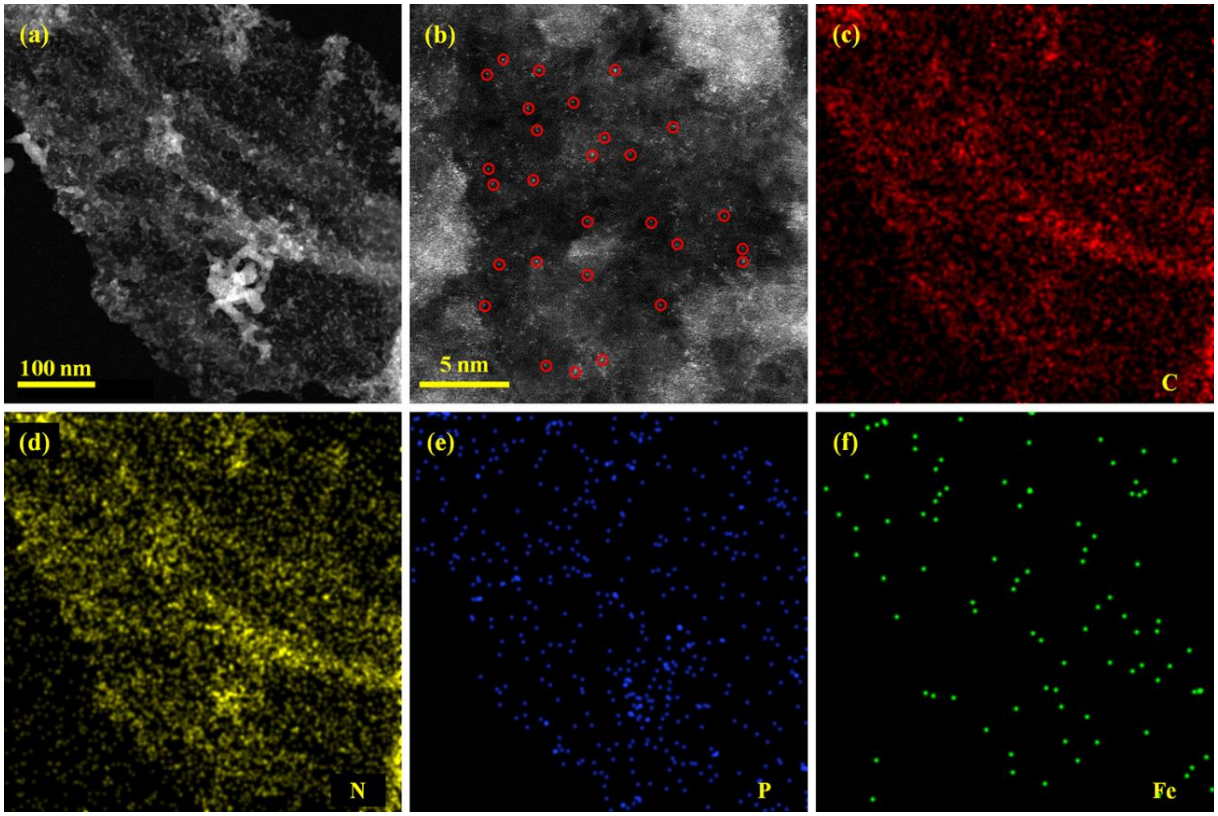

Figure 5. Aberration-corrected HAADF-STEM images and element mappings of Fe-NPC-L. Some of the isolated Fe atoms are highlighted by red circles in (b).

Fe-O-P, N-C and P-C bonds (denoted as Fe-N-P-C complex) is possibly formed on the surface of Fe-NPC, which may lead to the extraordinary ORR activity displayed above.

To further assess the contribution of the two type of possible active sites (encapsulated Fe_xP particles and Fe-N-P-C complex) towards the extraordinary overall ORR activity of Fe-NPC, Fe-NPC-L (with lower Fe loading), Fe_xP/C (with higher Fe loading) and NPC (without Fe) were employed as reference catalysts. The detailed Fe and P loadings of these materials were also obtained from the XRF and TPO analysis and the results are shown in Table S4. The aberration-corrected HAADF-STEM images of Fe-NPC-L are shown in Figure 5. No obvious particles can be observed in the dark field image of Fe-NPC-L, which may be owing to the low Fe and P loadings. In the element mapping, C, N, P and Fe are all evenly distributed throughout the whole catalyst,

and no accumulation can be observed. Fe single atoms can still be observed in high-magnification images (Figure 5b). The results suggest that Fe is uniformly distributed as single atoms on Fe-NPC-L. XPS survey of Fe-NPC-L is shown in Figure S4a, and the element concentrations are summarized in Table S2. The deconvolution of N 1s, P 2p and Fe 2p peaks of Fe-NPC-L are shown in Figure S4b-d and related component peak concentrations are summarized in Table S3. Since Fe-NPC-L was produced with the same method of Fe-NPC, the single Fe atoms on Fe-NPC-L should have similar coordination to N and P and form Fe-N-P-C complex on the surface. It is confirmed by the XANES spectra of Fe-NPC-L very similar to the one of Fe-NPC as shown in Figures 4a and 4b, and more detailed plot in Figure S12, in which there are two peaks with similar area that can be possibly assigning to Fe-N and Fe-P (Figure S12c). Thus, Fe-NPC-L is a Fe-N-P-C complex structure abundant material without Fe_xP particles.

Fe-N_x coordination complex has been reported to be the ORR active centre [20,22,52]. For a comparison, Fe and N co-doped WB derived carbon (Fe-NC) without P doping is also produced with identical impregnation-pyrolysis method. Detailed characterization of Fe_xP/C and Fe-NC and NPC without Fe are presented in supporting information (sections S2-S4, respectively, and Figure S5-S9).

The LSV curves of these catalysts are shown in Figure S13. It can be easily observed that the ORR activities of these catalysts have a trend of Fe_xP/C < NPC < Fe-NPC-L ≈ 30 % Pt/C < Fe-NPC and the comparison of the E_{onset} and E_{half} of these materials is shown in Figure 6. The carbon encapsulated iron phosphide (Fe_xP/C) showed the lowest activity, which is worse than metal free N-P co-doped carbon catalysts. It suggests that Fe_xP particles have minor contribution to the total activity of Fe-NPC. In addition, Fe_xP/C, NPC, Fe-NC and Fe-NPC-L possess similar pyridinic N concentration (higher than that of Fe-NPC), but these materials showed very different activity,

revealing that pyridinic N concentration is not a determining factor determining the ORR activity in Fe-NPC. When the single Fe atoms are integrated into N-P co-doped carbon (Fe-NPC-L), the activity boosted significantly, which is even comparable to that of 30 % Pt/C. When phosphorus is absent in the system (Fe-NC), the ORR activity was highly diminished and the E_{half} decreased

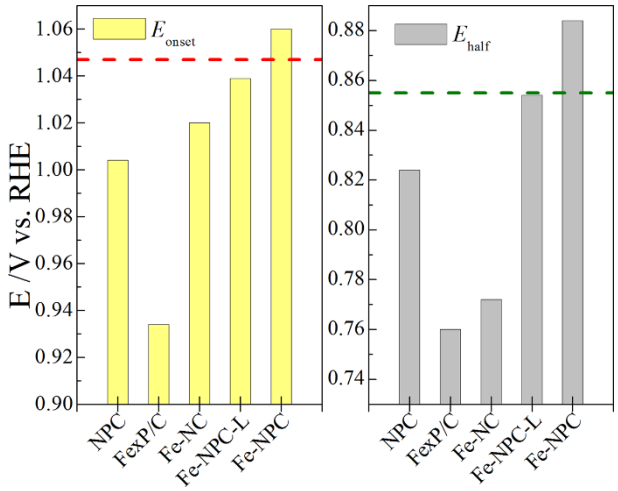

Figure 6. E_{onset} and E_{half} of NPC, Fe_xP/C, Fe-NC, Fe-NPC-L and Fe-NPC. Red and green dash line represent the E_{onset} and E_{half} of 30 % Pt/C, respectively.

to the second lowest among all materials, as shown in Figure 6. Together with characterization results, comparative activity testing results reveal that the atomically dispersed Fe-N-P-C complex active site is highly active for ORR reaction. The activity of materials possessing both encapsulated Fe_xP particles and Fe-N-P-C complex structures were further enhanced and thus led to an outstanding ORR activity.

Further electrochemical characterizations were carried out for Fe-NPC to reveal the catalyst selectivity. The electron transfer number was calculated from the as-obtained LSV curves with different rotating speed and the related K-L plots, which are shown in Figures S14 and S15a. All K-L plots exhibit linear relationships between J^{-1} and $\omega^{-1/2}$, the average electron transfer number for Fe-NPC is 3.90, slightly lower than that of 30 % Pt/C (3.95), suggesting that the ORR catalysed

by Fe-NPC is carried out via an efficient four-electron pathway. CVs of Fe-NPC and 30 % Pt/C with a scan rate of 0.1 V/s were carried out for 5000 cycles, and the CV curves of them before and after cycling are shown in Figure S15b. Obvious shape and reduction peak position changes can be observed from the curves of Pt/C. The peak position shifted 45 mV towards negative after cycling, indicating a poor long-term stability. While the curves of Fe-NPC before and after cycling almost overlap and the ORR peak position remain the same. This result suggests a good stability for long-term oxygen reduction of Fe-NPC. Additionally, current-time curves at 0.7 V of Fe-NPC and Pt/C were recorded and 3 M CH_3OH was introduced after 400 s (indicated by the arrow), the results are shown in Figure S15c. Suffering the crossover effect, the current of Pt/C dropped dramatically after methanol was injected, only about 50 % of its initial current remained. While for Fe-NPC, the addition of methanol only affected the current density slightly when it was introduced and the current restored after 100 s.

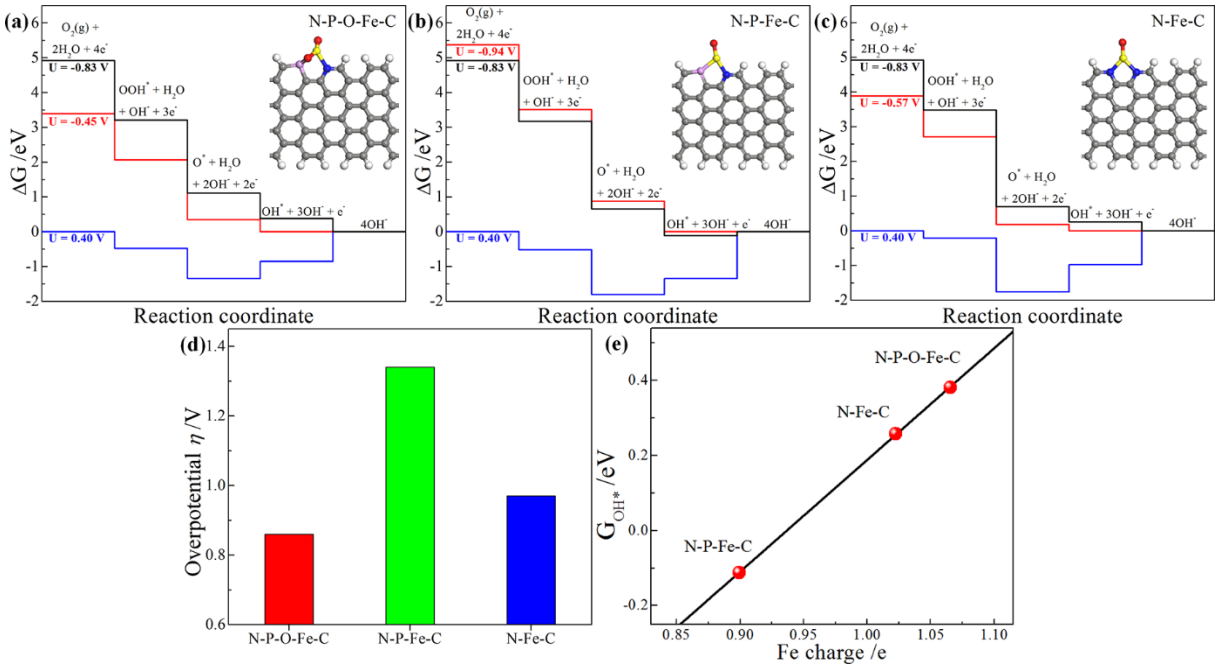

Figure 7. Free energy diagram for oxygen reduction reaction on the (a) N-P-O-Fe-C, (b) N-P-Fe-C and (c) N-Fe-C catalysts at the equilibrium potential (U= 0.40 V vs NHE), the zero cell potential

(U = -0.83V vs NHE) and the highest potential where all the reaction steps are exothermic. (d) The calculated ORR overpotentials (ηORR) of the three catalysts. (e) Trend in the adsorption free energy of OH* (GOH*) as a function of the Bader charge of the Fe atom of the three models.

To gain further insights into the superior ORR activity of the Fe-N-P-C complex structure, we resorted to first-principles calculations using density functional theory (DFT) methods (more computational details are shown in supplementary information). Since Fe-N, Fe-P, Fe-O-P, N-C and P-C bonds co-exist and considering the fact that nitrogen and phosphorus atoms, in particular due to the large size of P, prefer to substitute the C atoms near the edge [53,54], we constructed the corresponding model (a) in Figure S17, which contains all of the aforementioned bonds.

Another two possible models, model (b) and (c) in Figure S17, were also constructed, in which P-O bond or Fe-O bond instead of Fe-O-P bond is formed. Among these three models (model (a-c)),

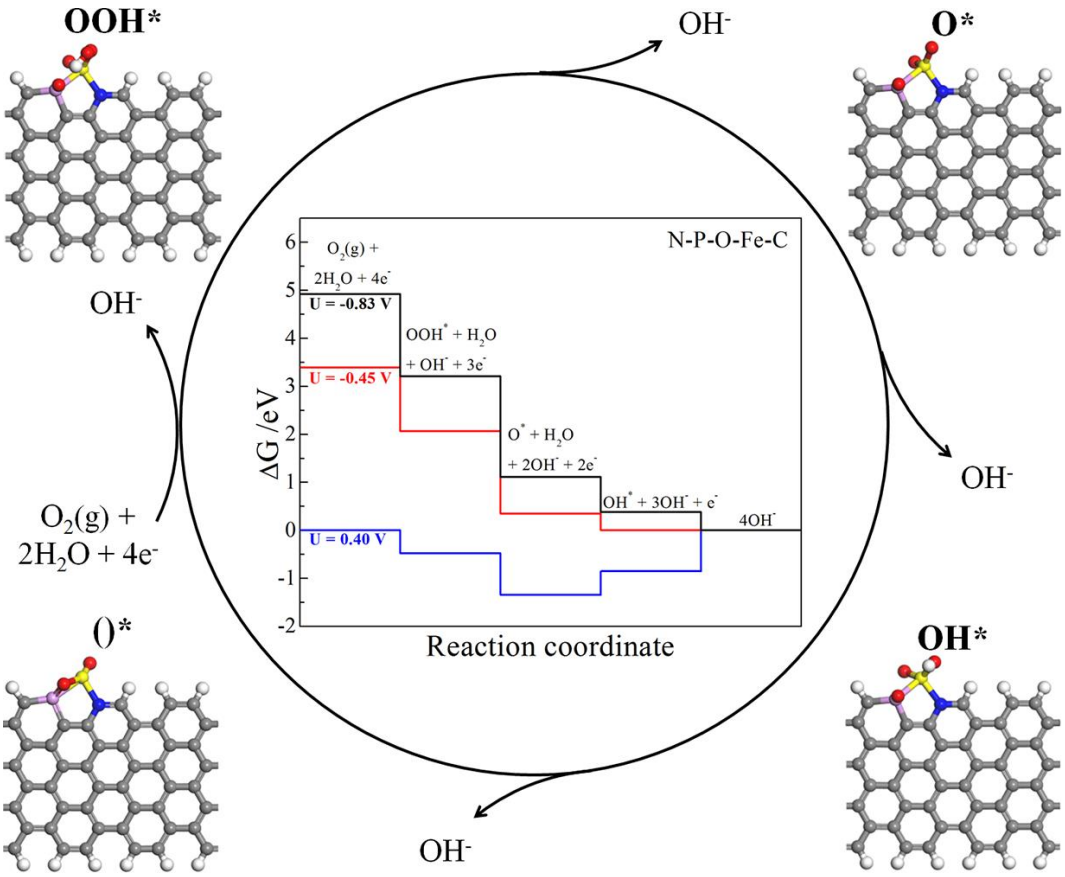

Figure 8. Schematic of the ORR on the N-P-O-Fe-C catalyst. The inset in cycle shows the free energy diagram for oxygen reduction reaction on this catalyst in alkali medium. For U < -0.45 V (vs. NHE), all steps are thermodynamically accessible.

model (a) is the most stable one, while the energies of the other two models are 0.34 eV and 0.69 eV higher than that of the model (a), respectively. Therefore, Fe-O-P bond is more likely to form on Fe-NPC, which is constant to the observations of XANES (Figure 4d). Moreover, a model with only Fe-P, Fe-N, P-C, N-C and adsorbed O (on Fe centre) and a classic model of Fe-N_2 coordination structure were also constructed for further comparison with the model (a). These two models are denoted as model (d) and model (e), respectively, as shown in Figure S17. It is reported that Fe sites are more likely to be the active site for ORR compare to N or C [55], we further

investigated the oxygen reduction progress based on the associative mechanism in alkaline media (equation S1- S6 in supporting information) on the Fe sites of model (a), (d) and (e). Figure 7a-c show the resulted free energy profiles of the three models. Since the ORR overpotential (η_{ORR}) is an important measure of the catalytic activity of a catalyst [56], the theoretical overpotentials of these three models for ORR were obtained from the correlated free energy profiles and compared in a bar chart (Figure 7d). It is clear that N-P-O-Fe-C (model (a)) possesses the lowest overpotential and thus the highest ORR activity. The rate determining step for these models is the desorption of OH*, which is similar to it on the Pt(111) surface [57,58].

The optimized configurations of the intermediates for the ORR on the model (a) (Figure 8) and the corresponding reaction pathway were further analysed to reveal the origin of its high ORR activity. At the ORR equilibrium potential, the formation of OOH* is exothermic, and ΔG is rather negative, suggesting a very fast reaction. Meanwhile, the O-O bond length is elongated to 1.42 Å for the OOH*, which allows an easy dissociation of O-O bond in the subsequent steps. This is further evidenced by the fact that the dissociation of OOH* to O* is strongly exothermic. The hydrogenation of O* is endothermic and the remove of OH* is even more endothermic, suggesting that the step of OH* removal is the rate-determining step that determines the overall ORR activity. Interestingly, the Fe-O-P bond of model (a) would break to form the isolated P-O bond during the ORR reaction and then Fe-O-P bond would be restored when an ORR catalytic cycle finished. During this dynamic redox process, the removal of OH* is facilitated that the free energy of this process reduced from 1.34 eV of model (d) (without Fe-O-P bond) to 0.85 eV of model (a), which leads to better ORR activity. To further understand the physical basis of the superior activity of the model (a), the electronic structures of the active sites of the three models, in principle determining the catalytic properties [59], were further analysed. Results (Figure 7e) reveal that the

electron properties of the active site indicated by Fe charge can be tuned by the surrounding local environments, like a mimic of natural catalysts such as cytochrome c oxidase [27]. The unique structure of N-P-O-Fe-C enlarge the Fe charge. A linear relationship between the G_{OH*} and the Fe charge was ambiguously observed in Figure 7e. Qualitatively, a more positive charge of the Fe atoms (model (a)) leads to a more mediate OH* adsorption (larger value of G_{OH*}), and thus to facilitate the overall ORR performance. Since model (a) is representing the possible configuration of Fe-N-P-C complex structure, the superior oxygen reduction activity of it may originate from the dynamic process of the Fe-O-P bonds during ORR. The results clearly demonstrated that the surrounding structure such as N and P coordinated to Fe govern the reactivity of the Fe active site.

Conclusion

In summary, we have demonstrated a general strategy of synthesizing atomically dispersed Fe-N-P-C electrocatalyst derived from biomass for electrochemical oxygen reduction. The as-prepared cost-effective catalyst exhibited remarkable ORR activity, long-term cycling stability and methanol tolerance in alkaline electrolyte, even outperformed most of state-of-the-art ORR catalysts. This outstanding performance has been mainly attributed to the atomically dispersed Fe-N-P-C complex active centres with Fe as the main active site, revealed by multiple catalyst characterization techniques such as aberration-corrected HAADF-STEM, XPS and XAFS. The new molecule-like structure has been proposed by systematic DFT calculations. In particular, the associated Fe-O-P bond plays a key role in lowering the stability of strongly adsorbed O* and OH* on the catalytically active sites, which can give rise to enhanced ORR performance. The atomically dispersion Fe-N-P-C complex structure is analogue to the nature catalysts where the reactivity of the metal active sites can be tuned by the coordination and ligands. The strategy demonstrated here illustrates a promising and efficient way to design the molecule-like heterogeneous ORR catalyst,

which could be widely applied in preparing various atomically dispersed, highly efficient catalysts in electrochemical energy technologies.

Reference

1 Miura, A. *et al.* Nitrogen-Rich Manganese Oxynitrides with Enhanced Catalytic Activity in the Oxygen Reduction Reaction. *Angew. Chem., Int. Ed.* **55**, 7963-7967, (2016).

2 Allendorf, M. D. Oxygen reduction reaction: A framework for success. *Nat. Energy* **1**, 16058, (2016).

3 Lefèvre, M., Proietti, E., Jaouen, F. & Dodelet, J.-P. Iron-based catalysts with improved oxygen reduction activity in polymer electrolyte fuel cells. *Science* **324**, 71-74, (2009).

4 Gong, K., Du, F., Xia, Z., Durstock, M. & Dai, L. Nitrogen-doped carbon nanotube arrays with high electrocatalytic activity for oxygen reduction. *Science* **323**, 760-764, (2009).

5 Yasuda, S., Furuya, A., Uchibori, Y., Kim, J. & Murakoshi, K. Iron-Nitrogen-Doped Vertically Aligned Carbon Nanotube Electrocatalyst for the Oxygen Reduction Reaction. *Adv. Funct. Mater.* **26**, 738-744, (2016).

6 Dai, L., Xue, Y., Qu, L., Choi, H. J. & Baek, J. B. Metal-free catalysts for oxygen reduction reaction. *Chem Rev* **115**, 4823-4892, (2015).

7 Yu, L., Pan, X., Cao, X., Hu, P. & Bao, X. Oxygen reduction reaction mechanism on nitrogen-doped graphene: A density functional theory study. *J. Catal.* **282**, 183-190, (2011).

8 Dubau, L. *et al.* Defects do Catalysis: CO Monolayer Oxidation and Oxygen Reduction Reaction on Hollow PtNi/C Nanoparticles. *ACS Catal.* **6**, 4673-4684, (2016).

9 Choi, D. S., Robertson, A. W., Warner, J. H., Kim, S. O. & Kim, H. Low-Temperature Chemical Vapor Deposition Synthesis of Pt-Co Alloyed Nanoparticles with Enhanced Oxygen Reduction Reaction Catalysis. *Adv. Mater.* **28**, 7115-7122 (2016).

10 Choi, K. H. *et al.* A simple synthesis of urchin-like Pt-Ni bimetallic nanostructures as enhanced electrocatalysts for the oxygen reduction reaction. *Chem. Commun.* **52**, 597-600, (2016).

11 Kuttiyiel, K. A. *et al.* Janus structured Pt-FeNC nanoparticles as a catalyst for the oxygen reduction reaction. *Chem. Commun.* **53**, 1660-1663, (2017).

12 Yu, H. *et al.* Nitrogen-Doped Porous Carbon Nanosheets Templated from g-C3 N4 as Metal-Free Electrocatalysts for Efficient Oxygen Reduction Reaction. *Adv. Mater.* **28**, 5080-5086, (2016).

13 Tao, L. *et al.* Edge-rich and dopant-free graphene as a highly efficient metal-free electrocatalyst for the oxygen reduction reaction. *Chem. Commun.* **52**, 2764-2767, (2016).

14 Zhang, J. *et al.* N,P-Codoped Carbon Networks as Efficient Metal-free Bifunctional Catalysts for Oxygen Reduction and Hydrogen Evolution Reactions. *Angew. Chem. Int. Ed.* **55**, 2230-2234, (2016).

15 Zhang, J., Zhao, Z., Xia, Z. & Dai, L. A metal-free bifunctional electrocatalyst for oxygen reduction and oxygen evolution reactions. *Nat. Nanotechnol.* **10**, 444-452, (2015).

16 Muthukrishnan, A., Nabae, Y., Okajima, T. & Ohsaka, T. Kinetic Approach to Investigate the Mechanistic Pathways of Oxygen Reduction Reaction on Fe-Containing N-Doped Carbon Catalysts. *ACS Catal.* **5**, 5194-5202, (2015).

17 Singh, K. P., Bae, E. J. & Yu, J. S. Fe-P: a new class of electroactive catalyst for oxygen reduction reaction. *J. Am. Chem. Soc.* **137**, 3165-3168, (2015).

18 Liang, Y. *et al.* Co_3O_4 nanocrystals on graphene as a synergistic catalyst for oxygen reduction reaction. *Nat. Mater.* **10**, 780-786, (2011).

19 Ma, M. *et al.* Biomass-Derived Porous Fe_3C/Tungsten Carbide/Graphitic Carbon Nanocomposite for Efficient Electrocatalysis of Oxygen Reduction. *ACS Appl. Mater. Interfaces* **8**, 32307-32316, (2016).

20 Jiang, W. J. *et al.* Understanding the High Activity of Fe-N-C Electrocatalysts in Oxygen Reduction: Fe/Fe_3C Nanoparticles Boost the Activity of Fe-N_x. *J. Am. Chem. Soc.* **138**, 3570-3578, (2016).

21 Li, R., Wei, Z. & Gou, X. Nitrogen and Phosphorus Dual-Doped Graphene/Carbon Nanosheets as Bifunctional Electrocatalysts for Oxygen Reduction and Evolution. *ACS Catal.* **5**, 4133-4142, (2015).

22 Ferrero, G. A. *et al.* Fe-N-Doped Carbon Capsules with Outstanding Electrochemical Performance and Stability for the Oxygen Reduction Reaction in Both Acid and Alkaline Conditions. *ACS Nano* **10**, 5922-5932, (2016).

23 Cui, X. *et al.* Pyridinic-Nitrogen-Dominated Graphene Aerogels with Fe-N-C Coordination for Highly Efficient Oxygen Reduction Reaction. *Adv. Funct. Mater.* 26, 5708-5717, (2016).

24 Zhu, C. *et al.* Self-Assembled Fe-N-Doped Carbon Nanotube Aerogels with Single-Atom Catalyst Feature as High-Efficiency Oxygen Reduction Electrocatalysts. *Small* **13**, 1603407 (2017).

25 Wang, J., Wang, K., Wang, F.-B. & Xia, X.-H. Bioinspired copper catalyst effective for both reduction and evolution of oxygen. *Nat. Commun.* **5**, 5285, (2014).

26 Suntivich, J. *et al.* Design principles for oxygen-reduction activity on perovskite oxide catalysts for fuel cells and metal–air batteries. *Nat. Chem.* **3**, 546–550, (2011).

27 Kim, E. *et al.* Superoxo, μ-peroxo, and μ-oxo complexes from heme/O_2 and heme-Cu/O_2 reactivity: Copper ligand influences in cytochrome c oxidase models. *Proc. Natl. Acad. Sci. U. S. A.* **100**, 3623-3628, (2003).

28 Zagal, J. H. & Koper, M. T. Reactivity Descriptors for the Activity of Molecular MN4 Catalysts for the Oxygen Reduction Reaction. *Angew. Chem. Int. Ed.* **55**, 14510-14521, (2016).

29 Ressler, T. WinXAS: a program for X-ray absorption spectroscopy data analysis under MS-Windows. *J. Synchrotron Radiat.* **5**, 118-122, (1998).

30 Ankudinov, A., Ravel, B., Rehr, J. & Conradson, S. Real-space multiple-scattering calculation and interpretation of x-ray-absorption near-edge structure. *Phys. Rev. B* **58**, 7565-7576, (1998).

31 Lou, F. *et al.* One-step electrochemical synthesis of tunable nitrogen-doped graphene. *J. Mater. Chem. A* **4**, 1233-1243, (2016).

32 Zhang, R., Zhang, C. & Chen, W. FeP embedded in N, P dual-doped porous carbon nanosheets: an efficient and durable bifunctional catalyst for oxygen reduction and evolution reactions. *J. Mater. Chem. A* **4**, 18723-18729, (2016).

33 Chen, K., Huang, X., Wan, C. & Liu, H. Hybrids based on transition metal phosphide (Mn_2P, Co_2P, Ni_2P) nanoparticles and heteroatom-doped carbon nanotubes for efficient oxygen reduction reaction. *RSC Adv.* **5**, 92893-92898, (2015).

34 Hu, Y. *et al.* Hollow spheres of iron carbide nanoparticles encased in graphitic layers as oxygen reduction catalysts. *Angew. Chem., Int. Ed.* **53**, 3675-3679, (2014).

35 Xiao, M., Zhu, J., Feng, L., Liu, C. & Xing, W. Meso/Macroporous Nitrogen-Doped Carbon Architectures with Iron Carbide Encapsulated in Graphitic Layers as an Efficient and Robust Catalyst for the Oxygen Reduction Reaction in Both Acidic and Alkaline Solutions. *Adv. Mater.* **27**, 2521-2527, (2015).

36 Jiang, H. *et al.* Nitrogen and phosphorus dual-doped hierarchical porous carbon foams as efficient metal-free electrocatalysts for oxygen reduction reactions. *Chemistry* **20**, 3106-3112, (2014).

37 Yang, D. S., Bhattacharjya, D., Inamdar, S., Park, J. & Yu, J. S. Phosphorus-doped ordered mesoporous carbons with different lengths as efficient metal-free electrocatalysts for oxygen reduction reaction in alkaline media. *J. Am. Chem. Soc.* **134**, 16127-16130, (2012).

38 Li, M. *et al.* Hybrid carbon nanowire networks with Fe–P bond active site for efficient oxygen/hydrogen-based electrocatalysis. *Nano Energy* **33**, 221-228, (2017).

39 Gil, E., Cortés, J., Iturriza, I. & Ordás, N. XPS and SEM analysis of the surface of gas atomized powder precursor of ODS ferritic steels obtained through the STARS route. *Appl. Surf. Sci.* **427**, 182-191, (2018).

40 Reddy, G. K., Boolchand, P. & Smirniotis, P. G. Unexpected Behavior of Copper in Modified Ferrites during High Temperature WGS Reaction—Aspects of $Fe^{3+} \leftrightarrow Fe^{2+}$ Redox Chemistry from Mössbauer and XPS Studies. *J. Phys. Chem. C* **116**, 11019-11031, (2012).

41 Peng, Y. *et al.* Probing the influence of the center atom coordination structure in iron phthalocyanine multi-walled carbon nanotube-based oxygen reduction reaction catalysts by X-ray absorption fine structure spectroscopy. *J. Power Sources* **291**, 20-28, (2015).

42 Yang, J., Liu, D.-J., Kariuki, N. N. & Chen, L. X. Aligned carbon nanotubes with built-in FeN 4 active sites for electrocatalytic reduction of oxygen. *Chem. Commun.* 329-331, (2008).

43 Kramm, U. I. *et al.* On an easy way to prepare metal–nitrogen doped carbon with exclusive presence of MeN4-type sites active for the ORR. *J. Am. Chem. Soc.* **138**, 635-640, (2016).

44 L, Y. *et al.* EXAFS study of $Mn_{1.28}Fe_{0.67}P_{0.46}Si_{0.54}$ compound with first-order phase transition. *J. Electron Spectrosc. Relat. Phenom.* **196**, 104-109, (2014).

45 Demirkiran, H., Hu, Y., Zuin, L., Appathurai, N. & Aswath, P. B. XANES analysis of calcium and sodium phosphates and silicates and hydroxyapatite–Bioglass® 45S5 co-sintered bioceramics. *Mater. Sci. Eng. C* **31**, 134-143, (2011).

46 Lin, Y. *et al.* Defective Carbon–CoP Nanoparticles Hybrids with Interfacial Charges Polarization for Efficient Bifunctional Oxygen Electrocatalysis. *Adv. Energy Mater.* 1703623, (2018).

47 Kruse, J. *et al.* Phosphorus $L_{2,3}$-edge XANES: overview of reference compounds. *J. Synchrotron Radiat.* **16**, 247-259, (2009).

48 Yang, S. *et al.* Soft X-ray XANES studies of various phases related to $LiFePO_4$ based cathode materials. *Energy Environ. Sci.* **5**, 7007-7016, (2012).

49 Lv, X. *et al.* Fe_2TiO_5-incorporated hematite with surface P-modification for high-efficiency solar water splitting. *Nano Energy* **32**, 526-532, (2017).

50 Yang, H. B. *et al.* Identification of catalytic sites for oxygen reduction and oxygen evolution in N-doped graphene materials: Development of highly efficient metal-free bifunctional electrocatalyst. *Sci. Adv.* **2**, e1501122, (2016).

51 Chen, P. *et al.* Atomically dispersed iron–nitrogen species as electrocatalysts for bifunctional oxygen evolution and reduction reactions. *Angew. Chem. Int. Ed.* **56**, 610-614, (2017).

52 He, F. *et al.* Ionic liquid-derived Fe–N/C catalysts for highly efficient oxygen reduction reaction without any supports, templates, or multi-step pyrolysis. *J. Mater. Chem. A* **4**, 6630-6638, (2016).

53 Chai, G.-L. *et al.* Active sites engineering leads to exceptional ORR and OER bifunctionality in P, N Co-doped graphene frameworks. *Energy Environ. Sci.* **10**, 1186-1195, (2017).

54 Li, M., Zhang, L., Xu, Q., Niu, J. & Xia, Z. N-doped graphene as catalysts for oxygen reduction and oxygen evolution reactions: Theoretical considerations. *J. Catal.* **314**, 66-72, (2014).

55 Chen, X., Yu, L., Wang, S., Deng, D. & Bao, X. Highly active and stable single iron site confined in graphene nanosheets for oxygen reduction reaction. *Nano Energy* **32**, 353-358, (2017).

56 Nørskov, J. K. *et al.* Origin of the overpotential for oxygen reduction at a fuel-cell cathode. *J. Phys. Chem. B* **108**, 17886-17892, (2004).

57 Tripković, V., Skúlason, E., Siahrostami, S., Nørskov, J. K. & Rossmeisl, J. The oxygen reduction reaction mechanism on Pt(111) from density functional theory calculations. *Electrochim. Acta* **55**, 7975-7981, (2010).

58 Nilekar, A. U. & Mavrikakis, M. Improved oxygen reduction reactivity of platinum monolayers on transition metal surfaces. *Surf. Sci.* **602**, L89-L94, (2008).

59 Nørskov, J. K., Bligaard, T., Rossmeisl, J. & Christensen, C. H. Towards the computational design of solid catalysts. *Nat. Chem.* **1**, 37-46, (2009).